International Journal of Nanomedicine

Dovepress
Taylor & Francis Group

Open Access Full Text Article

ORIGINAL RESEARCH

Multifunctional Poly(Acrylic Acid)-Coated $EuBiGd_2O_3$ Nanocomposite as an Effective Contrast Agent in Spectral Photon Counting CT, MRI, and Fluorescence Imaging

Yusuf O Ibrahim[1,2], Nabil Maalej[1,2], Aamir Younis Raja[1], Ahsanulhaq Qurashi[3], Mohamed Rahmani[4,8], Thenmozhi Venkatachalam[4], Osama Abdullah[5], Haidee J Paterson[5], Gobind Das[1], Curtis C Bradley[1], Rasha A Nasser[6], Charalampos Pitsalidis[1,7,8]

[1]Department of Physics, Khalifa University of Science and Technology, Abu Dhabi, 127788, United Arab Emirates; [2]Functional Biomaterials Group, Khalifa University of Science and Technology, Abu Dhabi, 127788, United Arab Emirates; [3]Department of Chemistry, Khalifa University of Science and Technology, Abu Dhabi, 127788, United Arab Emirates; [4]Department of Biological Sciences, College of Medicine & Health Sciences, Khalifa University, Abu Dhabi, 127788, United Arab Emirates; [5]Core Technology Platform Operations, New York University Abu Dhabi, Abu Dhabi, 129188, United Arab Emirates; [6]Department of Biomedical Engineering and Biotechnology, Khalifa University of Science and Technology, Abu Dhabi, 127788, United Arab Emirates; [7]Advanced Research and Innovation Center (ARIC) Khalifa University, Abu Dhabi, 127788, United Arab Emirates; [8]Center for Biotechnology, Khalifa University, Abu Dhabi, 127788, United Arab Emirates

Correspondence: Nabil Maalej, Email nabil.maalej@ku.ac.ae

Introduction: Recently, diagnostic methods based on multimodal and non-invasive imaging, such as MRI and CT scanners, have been developed for accurate cancer diagnosis. A key limitation of these imaging systems is their low contrast. Therefore, developing stable, non-toxic, and efficient multimodal imaging contrast agents is desirable. In this work, we demonstrated the synthesis of a poly (acrylic acid) (PAA) – coated nanoparticles (NPs), PAA@$EuBiGd_2O_3$-NPs as an imaging agent for contrast enhancement in spectral photon-counting computed tomography (SPCCT), magnetic resonance imaging (MRI) and fluorescence imaging (FL).

Methods: We synthesized PAA-coated $EuBiGd_2O_3$-NPs using a polyol method by dissolving metal nitrates and PAA in triethylene glycol. NaOH solution was added under constant heating at 180°C. The nanoparticles were precipitated with the addition of ethanol, then washed, dried, calcined at 600°C, and redispersed in water for further studies. The nanoparticles were characterized using TEM, SEM, XRD, XPS, FTIR, and PL spectroscopy. PAA@$EuBiGd_2O_3$-NPs were tested in vitro for their cytocompatibility with lung cancer epithelial cells (A549). The nanocomposite image contrast enhancement was evaluated using SPCCT, MRI, and FL imaging.

Results: The cell viability study showed that PAA@$EuBiGd_2O_3$-NPs is safe up to 250 µg/mL, exhibiting IC50 values of 365.8 and 337.8 µg/mL after 24 and 48 hours, respectively. The NPs have strong X-ray attenuation with a slope of ~61 HUmL/mg, as determined from the SPCCT concentration-dependent analysis. The MRI of the NPs reveals a high T1 contrast with a relaxivity of 11.77 $mM^{-1}s^{-1}$. Fluorescence imaging of cells incubated with PAA@$EuBiGd_2O_3$-NPs shows strong red luminescence.

Conclusion: The new nanocomposite has proven to be an effective trimodal contrast agent with high attenuation in CT, enhanced T1 signal in MRI, and strong red luminescence in FL imaging with promising diagnostic capabilities.

Keywords: multifunctional nanoparticles, multimodal imaging, spectral photon-counting CT, magnetic resonance imaging, fluorescence imaging

Introduction

Cancer, particularly in its malignant form, continues to pose a significant threat to human health. As one of the main causes of death, it may soon overtake heart disease as a leading cause of death globally.[1,2] An effective early-stage cancer diagnostic technique is necessary for the timely treatment of patients. In recent years, much attention has been focused on developing early-stage cancer diagnosis methods using stand-alone or combined imaging modalities, which include ultrasound (US),

Received: 12 November 2024
Accepted: 11 March 2025
Published: 14 April 2025

Graphical Abstract

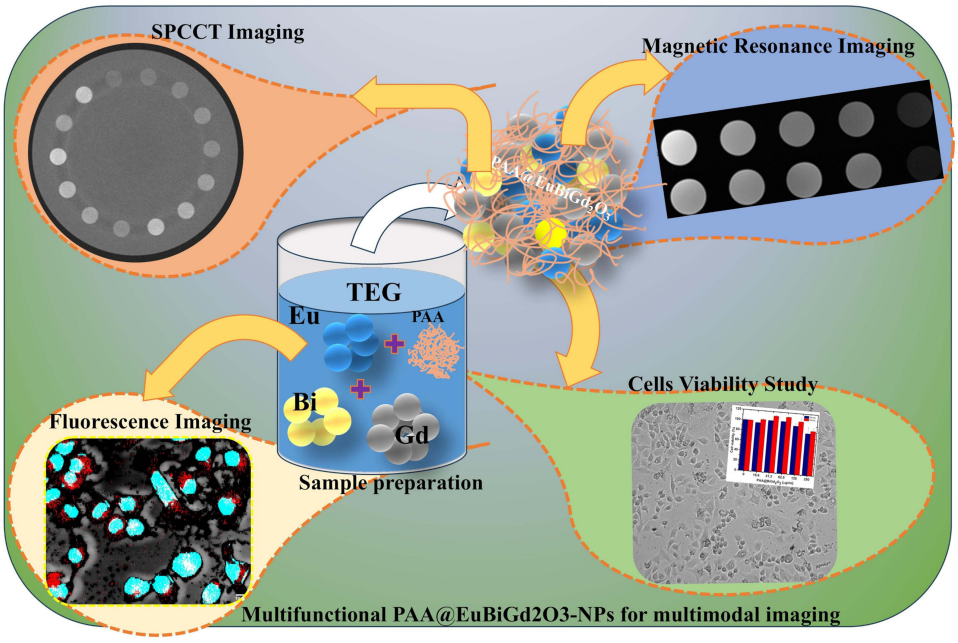

computed tomography (CT), magnetic resonance imaging (MRI), single-photon emission computed tomography (SPECT), and positron emission tomography (PET) imaging.[3,4] Spectral photon counting CT (SPCCT) is a relatively new imaging modality that employs energy-resolving detectors to generate multi-energy images with higher spatial resolution and better contrast than conventional CT and allows material identification and decomposition.[5] Magnetic resonance imaging (MRI) has been widely used in cancer diagnosis due to its high penetrating depth, non-ionizing radiation, and excellent soft tissue contrast. The MRI contrast can be further enhanced with contrast agents such as those containing gadolinium.[6–8] Computed tomography (CT) also provides 2D cross-sectional and 3D images with higher spatial resolution than MRI. However, the contrast of soft tissue in CT is low compared to MRI.[9–11] Fluorescence (FL) imaging, on the other hand, is ideal for imaging cells and tissues and has the best spatial resolution (hundreds of nanometers) with high sensitivity. However, due to its poor tissue penetration, FL imaging cannot capture anatomical 3D tissue structure in vivo.[12,13] To address these limitations and leverage the complementary strengths of the different imaging modalities, the multimodal imaging (MMI) approach has been introduced.[14,15] Most of these imaging modalities require the use of contrast agents to differentiate between normal and diseased tissues.

In recent years, nanoparticles (NPs) have received significant attention as contrast agents due to their distinctive properties, such as increased surface-to-volume ratio and better magnetic properties, which are useful in imaging, diagnosis, and therapy of diseases.[16–21] Among the nanoparticles, both metal-based and polymer-based nanoparticles have demonstrated significant potential in cancer diagnosis, owing to their unique physicochemical properties.[22] Polymer-based nanoparticles are valued for their controlled drug release, biocompatibility, and the ease with which they can be functionalized.[23,24] They have been extensively employed in imaging applications and drug delivery, offering targeted and prolonged contrast enhancement. Metal-based nanoparticles, especially those that contain transition metals[25–27] and lanthanide elements,[28–33] provide strong contrast for imaging techniques such as MRI and CT, which make them superior multimodal imaging agents. The incorporation of polymer coatings with metal nanoparticles further enhances their stability, biocompatibility, and functionality. In addition, Polymer functionalization also enhances the pharmacokinetics and biodistribution of metal nanoparticles.[34] The commonly used polymers for this purpose include

poly(acrylic acid),[35–37] poly(aspartic acid),[38–41] poly(ethylene glycol),[42–44] polysaccharides,[45,46] chitosan,[47,48] and poly (lactic-co-glycolic acid,[49–52].

Multifunctional NPs (MNPs) have received particular attention for their potential for facilitating the early diagnosis and effective treatment of cancer. MNPs can be used for MMI, and some are used for the dual purpose of imaging and therapy.[53–55] Hence, combining MRI, CT, and fluorescent nanoprobe into a single nanocomposite would yield a novel trimodal imaging contrast agent.

In order to design a multimodal contrast agent, we synthesized a tri-metal nanocomposite from Gadolinium (Gd), Bismuth (Bi), and Europium (Eu). These three metals have a high atomic number, high X-ray attenuation, and K-edge energies within the diagnostic X-ray spectrum.[56–58] In particular, Bi has the highest atomic number (Z = 83) and has been investigated as a CT contrast material.[59] Gd-based NPs have also been extensively applied as MRI contrast agents[60–66] with strong paramagnetic properties that significantly shorten the T1 relaxation times.[67,68] Europium is a rare earth material with bright luminescence properties in the red region and has been used for upconversion in fluorescence imaging.[69,70] However, the performance of most contrast agents currently used for MRI and CT imaging is limited by their toxicity, short imaging time, and low retention. To maintain biocompatibility and colloidal stability, the NPs must be coated with biocompatible hydrophilic ligands such as polyethylene glycol (PEG), Polyvinylpyrrolidone (PVP), Poly(acrylic acid) PAA, Polyvinyl alcohol (PVA) or bovine serum albumin (BSA).[71–75] In particular, PAA is a water-soluble polymer with high-binding capacity due to the presence of several carboxylic groups (COOH) per monomer, which can easily be used to conjugate the NPs with other functional materials such as dyes, targeting ligands and drugs.[76,77]

In this work, we used a modified polyol method to synthesize PAA-coated multifunctional NPs (PAA@EuBiGd$_2$O$_3$-NPs) as trimodal (MRI/SPCCT/FL) contrast agents with good colloidal stability and excellent biocompatibility. We demonstrated that the PAA@EuBiGd$_2$O$_3$-NPs have a high X-ray contrast in SPCCT, excellent T1 relaxation time in MRI, and bright red luminescence in FL imaging. The cytotoxicity study of the PAA@EuBiGd$_2$O$_3$-NP in vitro on the lung carcinoma epithelial cells (A549) showed low toxicity and good biocompatibility. Therefore, PAA@EuBiGd$_2$O$_3$-NP is a multimodal imaging contrast agent that can potentially enhance early cancer diagnosis. To our knowledge, the PAA@EuBiGd$_2$O$_3$-NPs have not been reported before as a trimodal contrast agent.

Methods

Materials

All chemicals used in the experiment are of analytical grade and were used as received. Gadolinium nitrate (Gd(NO$_3$)$_3$.6H$_2$O, 99%), Bismuth(III) nitrate pentahydrate (Bi(NO$_3$)$_3$·5H$_2$O, 99%), Europium(III) nitrate pentahydrate (Eu(NO$_3$)$_3$.6H$_2$O, 99%), sodium hydroxide (NaOH), triethylene glycol (TEG), ethanol and polyacrylic acid (PAA) were all obtained from Sigma-Aldrich Co. LLC. Washing of the NPs and suspension were done using triple distilled water with 18.2 MΩ resistivity.

Synthesis of PAA@EuBiGd$_2$O$_3$

PAA@EuBiGd$_2$O$_3$ NPs were synthesized using a modified polyol method. Briefly, a precursor solution (solution A) containing Bi(NO$_3$)$_3$·5H$_2$O (727.6 mg, 1.5 mmol), Eu(NO$_3$)$_3$.6H$_2$O (892 mg, 2 mmol), Gd(NO$_3$)$_3$·6H$_2$O (892 mg, 2 mmol) and 2 g of PAA (M_w= 2000) was prepared in 80 mL of TEG in a 250 mL three-neck flask. The mixture was stirred continuously at 80°C until it was completely dissolved. Another solution (solution B) of NaOH (1.6 g, 40 mmol) was prepared in 40 mL TEG and sonicated until a clear, uniform solution was obtained. Solution B was slowly added to solution A and kept at a temperature of 180°C for 12 hrs under constant stirring. After allowing the solution to cool to room temperature, 500 mL of ethanol was added and kept in the refrigerator until the NPs settled. The supernatant was removed to recover the NPs and washed with ethanol and distilled water three times each. Thereafter, the obtained NPs were dried at 80°C and then calcinated in the ashing furnace at 600°C for four hrs to obtain PAA@EuBiGd$_2$O$_3$-NPs. The calcinated NPs were ground into powder and redispersed in distilled water for further characterization and imaging studies. The PAA@Gd$_2$O$_3$ and PAA@BiGd$_2$O$_3$ were synthesized using their respective metal salts following the same steps.

 https://doi.org/10.2147/IJN.S506187

Characterizations

The synthesized PAA@EuBiGd$_2$O$_3$-NPs were characterized using different analytical techniques. The morphology and crystalline structure were studied using transmission electron microscopy (TEM), and high angle annular dark field-scanning transmission electron microscopy (HAADF-STEM) was performed with Tecnai TEM (Thermo Fisher Scientific, USA) operating at 200 kV voltage. Scanning electron microscopy, SEM (Phenom XL G2 Desktop SEM, Thermo Fisher Scientific, USA) equipped with energy dispersive X-ray spectroscopy (EDS) was used for morphology and elemental composition. The average nanoparticle size was measured using TEM imaging. The particle size distribution (hydrodynamic size) and the zeta potential of the nanoparticles were measured using a Nano ZA-90 Zetasizer (Malvern Instruments, Worcestershire, UK) utilizing dynamic light scattering (DLS). The phase structure and crystallinity of the compound were determined using Malvern PANalytical Empyrean diffractometer (Malvern PANalytical Ltd., United Kingdom) with an unfiltered Cu-Kα radiation (λ = 0.1540598 Å), 45 kV voltage, 40 mA current, a scan range of 2θ = 10–80°, and a scan step of 2θ = 0.013°. Furthermore, the diffraction mode of TEM was used to confirm the crystallinity of the sample. Various chemical and electronic states and interactions among the composite elements were obtained using X-ray photoelectron spectroscopy, XPS (XPS - Escalate Xi+, Thermo Fisher Scientific, USA) using a monochromatic Al-Kα radiation with binding energies well calibrated against that of adventitious carbon C1s, fixed at 284.6 eV. To investigate the successful grafting of PAA on the surface of the NPs, a Fourier transform-infrared (FT-IR) absorption spectrometer (Bruker Vertex 80v FT-IR, Germany) was used to record the FTIR absorption spectra. The photoluminescence (PL) and Raman spectra were obtained at an excitation wavelength of 488 nm for PL and 532 nm laser for the Raman, using the Witec Alpha 300 RAS Raman spectroscopy (WITec GmbH, Germany). The CIE 1931 diagram was used to obtain the x and y coordinates and the CIE chromaticity color diagram from the PL data.

SPCCT Phantom Imaging

To study the X-ray contrast enhancement properties of the PAA@EuBiGd$_2$O$_3$-NPs contrast agent, a MARS Microlab (5 × 120) scanner (MARS Bioimaging Ltd., Christchurch, New Zealand) was used. The scanner is equipped with a camera with 12 CdZnTe Medipix3RX chips, each with 128 × 128 pixels and 110 µm pitch, developed in collaboration with CERN.[78,79] The Medipix3RX detector is capable of separating X-ray photons based on their energies into up to eight energy bins. The scanner produces images corresponding to each energy bin.[80] This SPCCT scanner can be used to identify and quantify materials.[81] Using the SPCCT system, we scanned a Polymethyl Methacrylate (PMMA) cylindrical phantom of 12 cm diameter, containing 14 holes of 1 cm diameter for test tube inserts. We prepared different concentrations of PAA@Gd$_2$O$_3$-NPs (2, 4 and 8 mg/mL), PAA@BiGd$_2$O$_3$-NPs (5, 10, 15 and 20 mg/mL), PAA@EuBiGd$_2$O$_3$-NPs (5, 10, 15 and 20 mg/mL), and iodine (8 and 16 mg/mL) and placed them in 2 mL cylindrical polypropylene tubes that were inserted into phantom holes. The phantom was placed in the scanner gantry and scanned with the exposure parameters as indicated in Table 1. Image processing was performed on the collected raw data in DICOM format using the MARS scanner system software. Material decomposition (MD) was also performed on the material calibration phantom with the MARS CT built-in software (MARS MD)[82,83] using the same scanning protocol

Table 1 MARS Spectral CT Scanning Parameters

Parameters	Values
Tube current	40 µA
Tube voltage	118 kVp
Exposure time	160 ms
Projections/rotation	981
Energy bins (keV)	7–30, 30–49, 49–56, 56–65, 65–118
Slice thickness	0.1 mm
Voxel size	0.1 × 0.1 × 0.1 mm^3
Pixel pitch	110 µm
Filtration	0.125 mm Brass + 1.8 mm Al-equivalent filtration
Field of view (FOV)	128 mm

(Table 1) to generate material concentration images and compare the results with the actual concentration values obtained during the NP synthesis. The Hounsfield Unit (HU) of the material, NP concentration, is a scaled X-ray attenuation coefficient relative to water (HU):

$$HU = \left(\frac{\bar{\mu}_{NPs} - \bar{\mu}_w}{\bar{\mu}_w}\right) \times 1000 \quad (1)$$

Where $\bar{\mu}_{NPs}$ and $\bar{\mu}_w$ are the mean linear attenuation coefficients of the NPs and water, respectively. The relationship between the pixel values in HU and the various concentrations of the NP were assessed for the different SPCCT energy windows. A comparison was made between the image contrast obtained using the different NP concentrations and that obtained using different iodine concentrations.

Magnetic Resonance Measurement

Serial dilution of nanoparticle suspensions with various Gd-concentrations (0, 0.06, 0.125, 0.25, and 0.5 mM) was prepared with triple distilled water in a 5 mL Eppendorf tube. Samples were placed in a transmit/receive quadrature knee coil within a clinical 3T MRI scanner (MAGNETOM Prisma, Siemens Healthineers, Erlangen, Germany) for quantitative T1 relaxation mapping. A saturation recovery spin echo sequence was employed with the following parameters: variable repetition times (TR, in ms) of 150, 200, 300, 500, 800, 1000, 1500, 3000, 4000, and 8000 ms; echo time (TE) of 11 ms; field of view (FOV) of 130 mm × 130 mm; acquisition matrix of 320 × 320; and slice thickness of 3.5 mm. The acquired data was processed using MATLAB 2024a (MathWorks Inc.) with a custom script for pixel-by-pixel nonlinear least squares fitting (utilizing the lsqcurvefit function). The signal at each voxel was plotted against its corresponding TR, and a T1 recovery curve was fit using the $M\ (TR) = M_0\ (1 - e^{-TR/T1})$. The two unknowns, M_0 and T_1, were fitted for each voxel. T_1 values were reported in milliseconds (ms). Relaxivity values were determined from the plot of 1/T1 against the Gd concentrations.

Fluorescence Microscopy

A549 cells (1×10^5) were seeded on sterile poly-L-lysine-coated glass coverslips in a 6 well plate and incubated at 37 °C in a 5 % CO_2 incubator overnight. Cells were treated with 125 µg/mL of nanoparticle solutions (PAA@$EuBiGd_2O_3$) prepared in a serum-free medium (RPMI) for 24 hrs. The cells were washed with PBS and fixed with 4 % paraformaldehyde (PFA, Thermo Fisher Scientific) for 15 minutes at room temperature.

The cells were stained with 4′,6′-diamidino-2-phenylindole (DAPI) (Invitrogen). The slides were imaged using an epifluorescence/confocal microscope (Olympus FV3000 Confocal Microscope, Japan).

In vitro Cytotoxicity Measurements

Human lung cancer cell line A549 was purchased from American Type Culture Collection (ATCC) and cultured in Roswell Park Memorial Institute (RPMI) 1640 medium (Sigma) supplemented with 10% (v/v) of heat-inactivated fetal bovine serum (Sigma) and maintained at 37 °C in a fully humidified atmosphere containing 5 % CO_2. All experiments were performed on logarithmically growing cells. Cell growth and viability were assessed by CellTiter-Glo Luminescent Assay (Promega Corporation, USA) according to the manufacturer's instructions. In brief, A549 cells were seeded in triplicate in a 96-well plate at a density of 2×10^4 cells per well in 100 µL of media and cultured at 37 °C with 5 % CO_2 overnight. The next day, the cells were treated with varying concentrations of PAA@$EuBiGd_2O_3$-NPs (1000, 500, 250, 125, 62.5, 31.2, and 15.6 µg/mL) for 24 and 48 hours. Subsequently, 20 µL of the CellTiter-Glo® reagent was added and mixed in the shaking incubator at 350 rpm for 15 min, and the luminescence was measured using a GloMax® Discover luminometer.

Results and Discussion

Characterization of the Nanoparticles

The result of the X-ray diffraction (XRD) pattern affirmed the crystallinity of the synthesized PAA@$EuBiGd_2O_3$ -NPs. The XRD pattern shown in (Figure 1a(i), blue trace) is similar to that of $EuBiO_3$ reported (ICDD:1-083-4445) in (Figure 1a(ii), red trace) with a slight shift in the peaks. This shift could be attributed to the presence of Gd in the crystal

 https://doi.org/10.2147/IJN.S506187

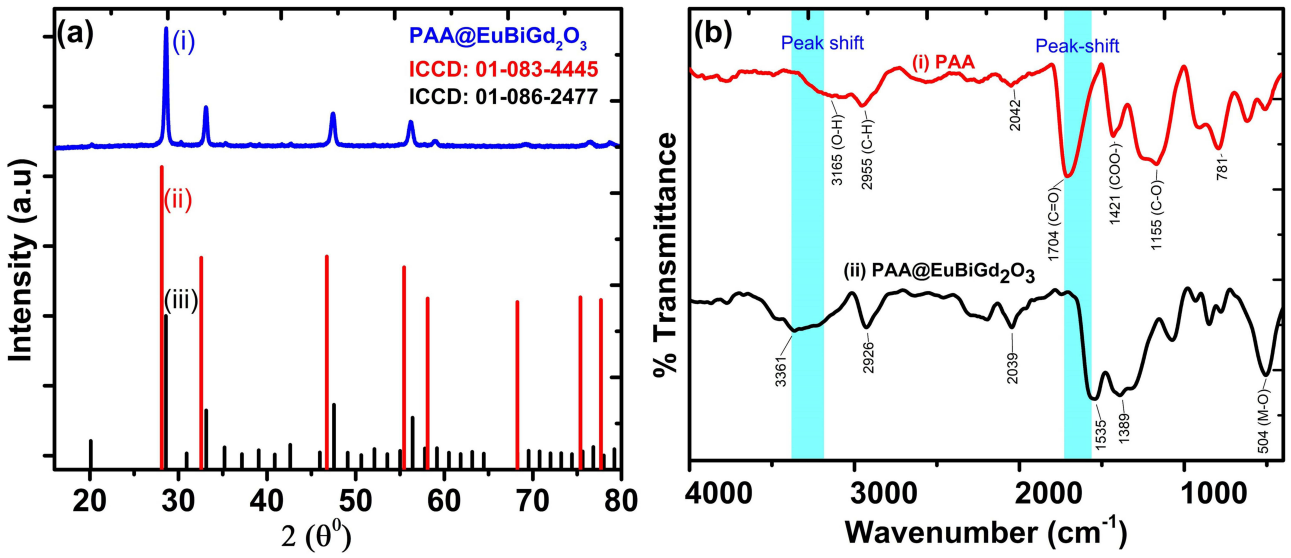

Figure 1 (**a**) The XRD pattern of (i) PAA@EuBiGd$_2$O$_3$ nanoparticles; (ii) EuBiO$_3$ (ICCD: 01-083-4445); and (iii) Gd$_2$O$_3$ (ICCD:01-086-2477). (**b**) FT-IR absorption spectra of (i) pure PAA (Mw = 2000 KDa); (ii) PAA-coated EuBiGd$_2$O$_3$ nanoparticles confirming the successful grafting of PAA on the surface of the trimetallic oxide.

structure. In addition, other smaller peaks are present and match the reported XRD spectra of Gd$_2$O$_3$ (ICDD: 01-086-2477) in (Figure 1a(iii), black trace). The crystallite size of 25.6 ± 2.3 nm was determined using the Debye-Scherrer equations:

$$D = \frac{K\lambda}{\beta \, Cos\, \theta} \tag{2}$$

Where D is the crystallite size of the NPs, K is the Debye–Sherrer shape factor (0.98), λ is the wavelength of the x-ray, and β is the FWHM, and θ is the Bragg's angle. This demonstrates a new crystal structure with Bi and Eu atoms incorporated into the matrix of Gd to form a single-phase material. To the best of our knowledge, this is the first report on the crystalline structure of EuBiGd$_2$O$_3$.

The FTIR was used to investigate the successful coating of the PAA on the surface of the NPs. The FTIR spectrum of the bare PAA (Figure 1b(i)) and PAA@EuBiGd$_2$O$_3$ NPs are shown in Figure 1b(ii) for comparison. The characteristic peak of PAA at 1704 cm^{-1} is recognized as the asymmetrical C=O stretching of the carboxylic acid group. A broad peak at 3165 cm^{-1} and 2955 cm^{-1} corresponds to the respective O-H stretch from water and C-H stretch from PAA.[84] In addition, the peaks located at 1155 cm^{-1} and 1421 cm^{-1} are attributed to the symmetric and anti-symmetric stretching vibration of C-O in COO-(carboxylate) groups. The successful binding of PAA onto the surface of the NPs via electrostatic bonding is evident in the FTIR spectrum of PAA@EuBiGd$_2$O$_3$. There are observable red-shifting of the peaks at 1704 cm^{-1} and 3165 cm^{-1} by 169 cm^{-1} and 196 cm^{-1}, respectively, due to the electrostatic bonds between the Gd^{3+} ions and the COO-group presence in PAA.[85,86] In addition, the peaks at 1704 cm^{-1} and 3165 cm^{-1} become more intense and broader. A peak at 504 cm^{-1} is attributed to the metal-oxide (M-O) stretching. This result is supported by many reported cases of carboxyl groups containing ligands coated on metal-oxide NPs.[87–90] The presence of this PAA in the NPs explains the good colloidal stability and biocompatibility reported in this study.

Furthermore, the EDS mapping from the SEM analysis (Figure S1) was used to analyze the elemental composition and distribution of the NPs. Figure S1a–f show that Eu, Bi, and Gd are evenly distributed, while carbon and oxygen accumulate on the nanoparticle's surface. It should be noted that the atomic and weight concentration of Gd are approximately twice that of Eu and Bi (Figure S1g). Hence, the formation of PAA@EuBiGd$_2$O$_3$-NPs was confirmed. The TEM microscopic images (Figure 2a) of the PAA@EuBiGd$_2$O$_3$-NPs reveal an uneven spherical-like shape with an average particle size of 24 ± 4 nm, determined from a log-normal fit of the particle size distribution (Figure 2d). Figure 2b shows the PAA@EuBiGd$_2$O$_3$ nanoparticles solution in water, confirming its stability. The uniform dispersion

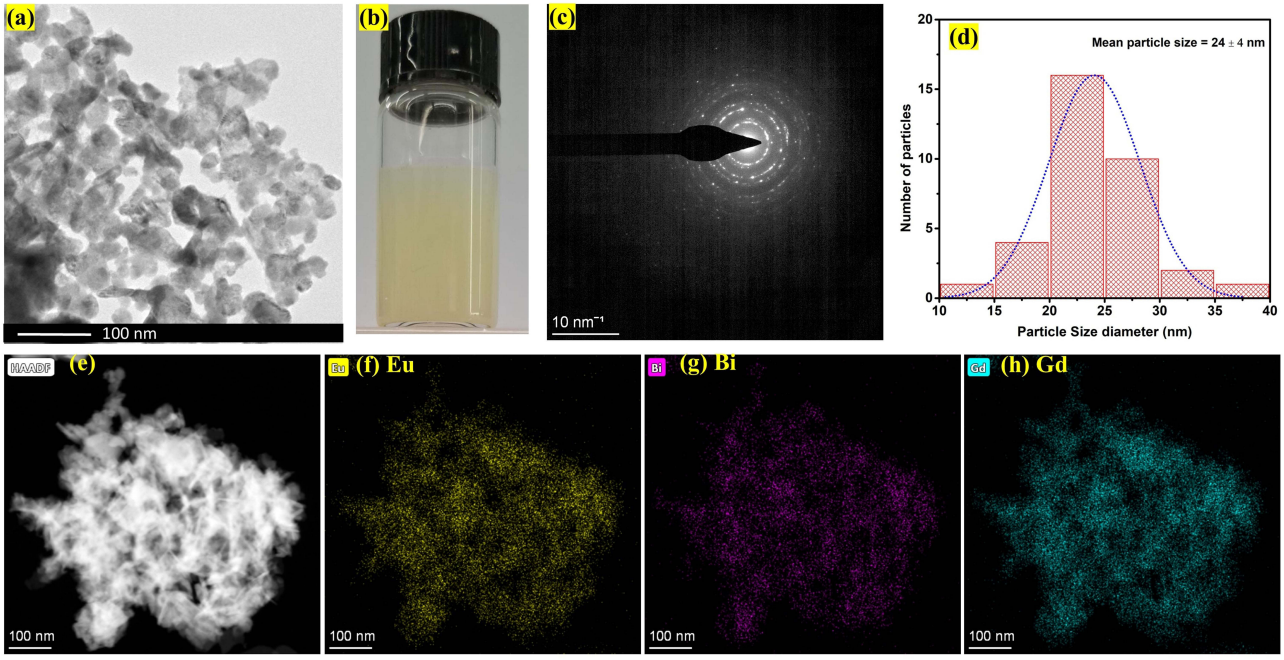

Figure 2 (**a**) Transmission electron Microscopy (TEM) images; (**b**) photo of PAA@EuBiGd$_2$O$_3$-NPs solution dispersed in water, (**c**) the selected area diffraction (SAED) pattern; (**d**) log-normal particle size distribution; (**e**) high-angle annular dark-field scanning transmission electron microscopy (HAADF-STEM) image; (**f–h**) element maps for Eu, Bi and Gd images of the PAA@EuBiGd$_2$O$_3$-NPs.

without visible aggregation or precipitation suggests good colloidal stability, likely due to the steric repulsion provided by the PAA coating.[91] Additionally, the stability in aqueous media indicates that the nanoparticles can remain well-dispersed under physiological conditions, enhancing their suitability for imaging applications. The SAED pattern (Figure 2c) displays bright spots, indicating the crystallinity of the nanoparticles. HAADF-STEM-EDX images (Figure 2e–h) demonstrate the uniform distribution of the key elements Eu, Bi, and Gd. In addition, an average particle size of 73.59 nm (PDI: 0.262) and a zeta potential of −29.0 mV were obtained from the particle size distribution analysis Figure S2a and b. The particle size measured by DLS is much larger than that obtained from TEM. This discrepancy arises because TEM provides a number-based size measurement, while DLS is intensity-based hydrodynamic size measurement, giving greater emphasis to larger particles in the distribution.[92]

The XPS analysis was used to investigate the various chemical states and the interactions among the composite elements. The XPS spectra of the composite material (PAA@Eu-BiGd$_2$O$_3$) are shown in Figure S3. The characteristic peaks of Eu, Bi, and Gd, as well as those of C and O, are evident in the survey spectra (Figure S3a). The high-resolution Gd 4d core level deconvoluted into two peaks, at 141.69 eV and 144.1 eV (Figure S3b), were ascribed to the Gd 4d$_{5/2}$ and Gd 4d$_{3/2}$ with spin-orbit separation of 2.41 eV. This separation corresponds to the 2.41 eV energy loss during the spin-orbit splitting of Gd 4d into Gd 4d$_{5/2}$ and Gd 4d$_{3/2}$. This confirms the presence of the Gd^{3+} valence state.[93,94] Similarly, the two deconvoluted Bi peaks located at 165.36 eV and 160.4 eV (Figure S3c) correspond to the Bi 4f$_{5/2}$ and Bi 4f$_{7/2}$ due to the spin-orbit coupling. In the Eu 3d core level, we observe Eu 3d$_{5/2}$ and Eu 3d$_{3/2}$ at binding energies of 1133.2 eV and 1163.5 eV, respectively (Figure S3d). These prominent features are attributed to the 3+ state of Eu.[95,96] As indicated in Figure S3e, the C 1s core level peak at 284.4 eV, which represents the C=C binding, was further deconvoluted into two different peaks at 286.2 and 288.2 eV, which correspond to the C-O and C=O oxygen-containing carbonaceous material. The single dominant peak in the O 1s spectrum (Figure S3f), located at 531.4 eV, is attributed to the bonding between O^{2-} and Gd^{3+} and/or other metals in the composite material. This O 1s dominant peak demonstrated three different peaks at 528.4 eV, 530.8 eV, and 532.9 eV, which are related to the lattice oxygen, adsorbed, and chemisorbed oxygen molecules in the Gd-O, respectively.[97,98]

https://doi.org/10.2147/IJN.S506187

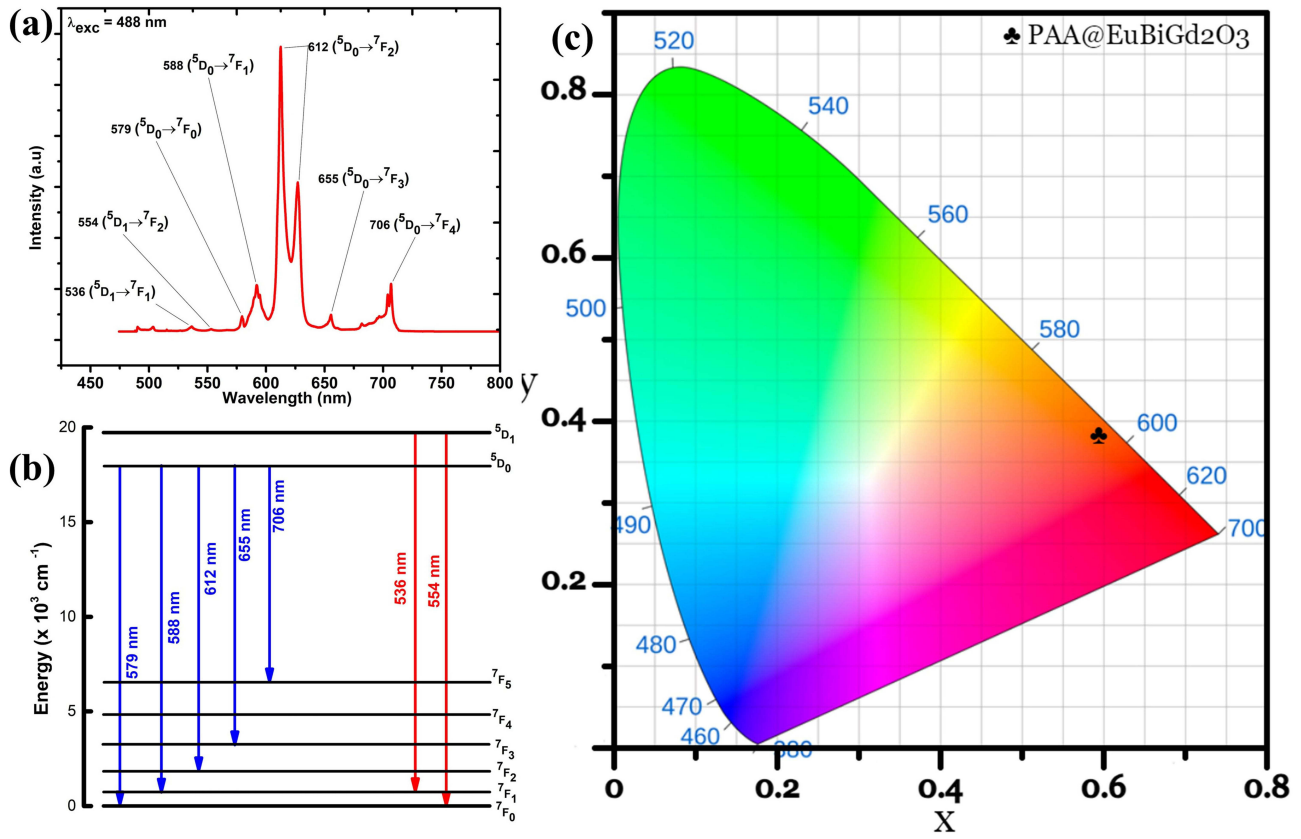

Figure 3 (**a**) Photoluminescence spectrum of PAA@EuBiGd$_2$O$_3$ excited at a wavelength of 488 nm showing red fluorescence; (**b**) Observed Photoluminescence energy transition diagram of Eu^{3+}; and (**c**) The CIE standard chromaticity diagram of PAA@EuBiGd$_2$O$_3$ excited at 488 nm.

Figure 3a shows the room temperature photoluminescence spectra of PAA@EuBiGd$_2$O$_3$ -NPs excited with laser light of 488 nm wavelengths. The NPs give a red luminescence with various intra-configurational transitions represented by their respective emission lines. The peaks centered at 536, 554, 579, 588, 612, 655, and 706 nm correspond to energy level transitions $^5D_1$ to $^7F_1$, $^5D_1$ to $^7F_2$, $^5D_0$ to $^7F_0$, $^5D_0$ to $^7F_1$, $^5D_0$ to $^7F_2$, $^5D_0$ to $^7F_3$, and $^5D_0$ to $^7F_4$ respectively.[99,100] The peak at 588 nm corresponding to the transition $^5D_0$ to $^7F_1$ is the only peak attributed to the magnetic transition.[101–103] Other transitions from $^5D_0$ to ^7F_j (j = 0, 3, and 5) have zero magnetic and electric dipole moments and are forbidden according to the selection rules. However, these transition peaks in the PL spectra are present due to crystal-field interaction, leaving those states in a mixed state. Other transitions, $^5D_1$ to $^7F_1$, $^5D_1$ to $^7F_2$, $^5D_0$ to $^7F_2$, and $^5D_0$ to $^7F_4$, correspond to the electric dipole transition. These types of transition for Eu^{3+} are shown in Table 2. Figure 3b and c show the observed photoluminescence energy transition diagram of Eu^{3+} and the CIE chromaticity diagram of

Table 2 The Peaks, Transitions, and Types of Transitions of Eu^{3+} in PAA@EuBiGd$_2$O$_3$

S/N	Peak (nm)	Transition	Types of transitions
1	536	$^5D_1 \rightarrow 7F_1$	Electric dipole
2	554	$^5D_1 \rightarrow {}^7F_2$	Electric dipole
3	579	$^5D_0 \rightarrow {}^7F_0$	Forbidden
4	588	$^5D_0 \rightarrow {}^7F_1$	Magnetic dipole
5	612	$^5D_0 \rightarrow {}^7F_2$	Electric dipole
6	655	$^5D_0 \rightarrow {}^7F_3$	Forbidden
7	706	$^5D_0 \rightarrow {}^7F_4$	Electric dipole

PAA@EuBiGd$_2$O$_3$-NPs obtained from CIE 1931 diagram software, using the PL data. This was used to evaluate the sample's exact emission color and color purity. The calculated x- and y-coordinates of the PAA@EuBiGd$_2$O$_3$ were at x = 0.592 and y = 0.382. The color coordinate is found to be in the pure red region, which shows that the PAA@EuBiGd$_2$O$_3$ NPs give appreciable emission in the red region, making them a good candidate for fluorescence imaging.

Phantom SPCCT Imaging

Using iterative reconstruction method, spectral CT images of the phantom containing various concentrations of Gd$_2$O$_3$ (2, 4, and 8 mg/mL), PAA@BiGd$_2$O$_3$ (5, 10 and 15 and 20 mg/mL), PAA@EuBiGd$_2$O$_3$ (5, 10 and 15 and 20 mg/mL), iodine (8 and 16 mg/mL), and water, as a reference, were obtained. The layout of the phantom with the different concentrations of contrast agents and the spectral CT images for the five energy windows are shown in Figure 4a–f. It is visible that the highest signal from Gd$_2$O$_3$, PAA@EuBiGd$_2$O$_3$, and PAA@EuBiGd$_2$O$_3$ was obtained for the third energy window (49 - 56 keV), which included the K-edge of gadolinium (50.2 keV). As expected, the highest contrast from iodine occurred in the second energy bin (30–49 keV), attributed to the K-edge of iodine at 33.7 keV. It is also evident that the attenuation of PAA@EuBiGd$_2$O$_3$ is more intense than that of PAA@BiGd$_2$O$_3$, and this is due to the contribution from the three high Z elements of Eu, Bi, and Gd present in the NP solutions.

To investigate the variation of the X-ray attenuation with different energy windows and the relationship between the HU and the concentrations of the NPs, a circular region of interest of 1 mm diameter was drawn inside each tube containing the contrast agents.

The mean value and the standard deviation of the pixel values were recorded using *ImageJ* software. The mean attenuation values were converted to HU using Equation 1. Figure 5a and b, show the plot of the HU for different energy windows and HU versus the concentrations for different materials. From the plot for Gd$_2$O$_3$, PAA@BiGd$_2$O$_3$, and PAA@EuBiGd$_2$O$_3$, it can be observed that the highest signal was obtained in the energy window (49–56 keV) that

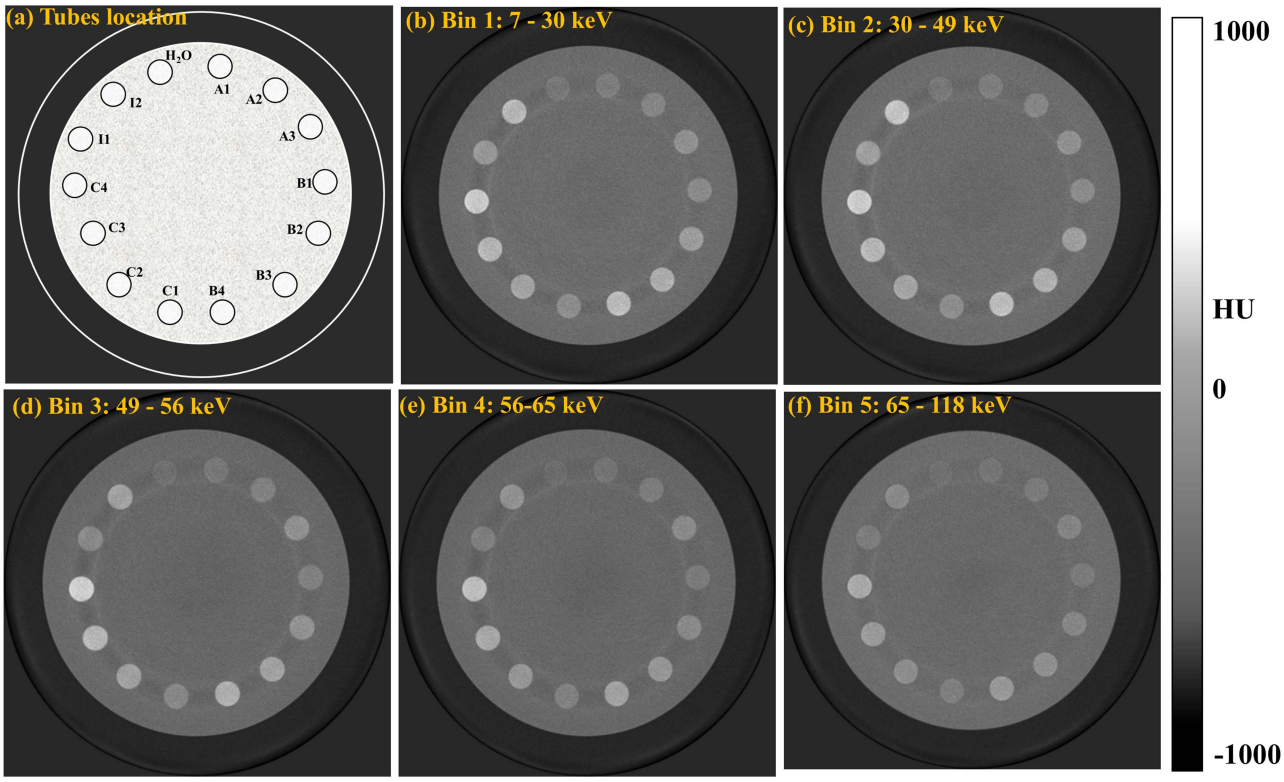

Figure 4 (**a**) The cylindrical materials phantom showing the locations of materials sample tubes containing water, Gd$_2$O$_3$ (A1, A2, and A3 correspond to 2, 4, and 8 mg/mL), PAA@BiGd$_2$O$_3$ (B1, B2, B3, and B4 correspond to 5, 10, 15, and 20 mg/mL), PAA@EuBiGd$_2$O$_3$ (C1, C2, C3 and C4 correspond to 5, 10, 15, and 20 mg/mL) and iodine (I8 and I16 correspond to 8 and 16 mg/mL); (**b–f**) CT images of the materials phantom for (**b**) 7–30, (**c**) 30–49, (**d**) 49–56, (**e**) 56–65 and (**f**) 65–118 keV energy windows.

https://doi.org/10.2147/IJN.S506187

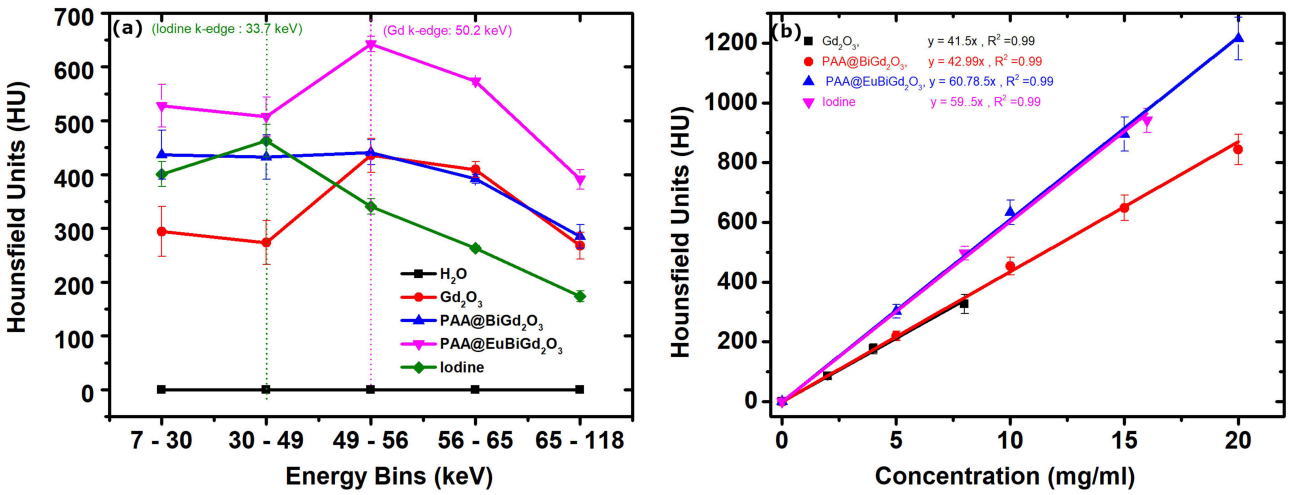

Figure 5 (**a**) A plot of HU for various energy windows for water, Gd_2O_3, PAA@$BiGd_2O_3$, PAA@$EuBiGd_2O_3$ and iodine; (**b**) A plot of HU versus concentrations for Gd_2O_3, PAA@$BiGd_2O_3$, PAA@$EuBiGd_2O_3$, and iodine.

contains the K-edge of Gd (50.2 keV), while for Iodine, the energy window 30–49 keV which contains the K-edge (30.2 keV) has the highest intensity. In addition, the signal is more intense for the PAA@$EuBiGd_2O_3$-NPs, which could be attributed to the presence of three high-atomic number materials of Eu, Bi, and Gd and the proximity of the K-edges of Eu (48.5 keV) and Gd (50.2 keV). This proves that the PAA@$EuBiGd_2O_3$-NPs are a better contrast agent in SPCCT imaging than iodine. Furthermore, the linear relationship between the HU and the nanoparticle concentrations is evident in Figure 5a. The X-ray attenuation increases linearly with increased concentrations for all the materials. The plot shows the best linear fit with R-squared values close to unity for all samples. The relationship between the X-ray attenuation of a contrast agent and its concentration can generally be described by a linear equation:

$$\bar{\mu}_{mixture} = C_w\bar{\mu}_w + C_{NP}\bar{\mu}_{NP} \tag{3}$$

where $\bar{\mu}_{NPs}$ and $\bar{\mu}_w$ are the mean attenuation from the nanoparticle material and water, respectively. C_w and C_{NP} are the ratios of water and the NP in the mixture. The values of the attenuation coefficients depend on the material and the energy windows. The slope of the linear equation mainly depends on the concentration of the high-Z NPs, C_{NP}. The PAA@$EuBiGd_2O_3$ plot of HU versus NP concentration exhibits the highest slope of about 61 HU/mg.mL^{-1}, which is a measure of its contrast enhancement property.

The MARS CT integrated software (MARS-MD) was used to obtain the material decomposition (MD).[104,105] Before this measurement, the different nanoparticle concentrations were used to calibrate the MARS-MD software. MARS MD images were used to obtain the material concentration by selecting an ROI for each material and measuring the mean concentration value. The material concentration values were compared with the known actual experimental values. Figure 6a presents the reconstructed material decomposition image showing the position of different NP concentrations in the phantom. Figure 6b–e shows the plot of the actual concentrations against the measured concentrations from the MD image for Gd_2O_3, PAA@$BiGd_2O_3$, PAA@$EuBiGd_2O_3$, and iodine. An excellent agreement between the actual and measured concentration was observed. This confirms the accuracy of the MARS-CT algorithm for material decomposition.

MRI Contrast Measurement

MRI contrast agents were assessed by their proton transverse and longitudinal relaxivities r_1 and r_2. The performance of PAA@$EuBiGd_2O_3$ NPs as MRI contrast agents was investigated at different concentrations in water. The signal brightness of the T1-weighted MR image increases with an increase in the concentration of Gd content in the NPs (Figure 7a and b). The r_1 values estimated from the plot of 1/T1 as a function of Gd concentration are 12.72 mM^{-1}s^{-1} and 11.77 mM^{-1}s^{-1} for Gd_2O_3 and PAA@$EuBiGd_2O_3$-NPs, respectively. The contrast enhancement and the relaxivity value of

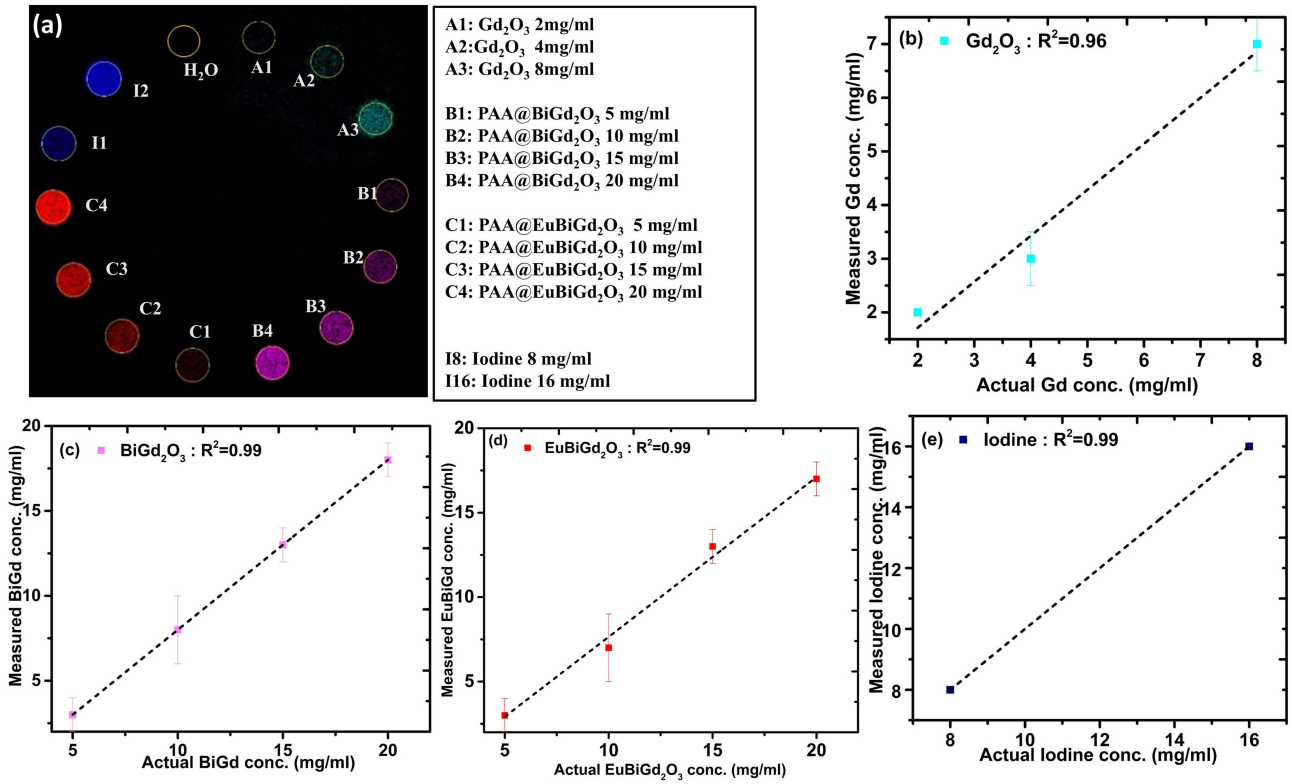

Figure 6 (**a**) Material decomposition image reconstructed from the MARS-MD. (**b–e**) Plots of measured versus actual concentrations for (**b**) Gd_2O_3, (**c**) PAA@$BiGd_2O_3$, (**d**) PAA@$EuBiGd_2O_3$, and (**e**) Iodine.

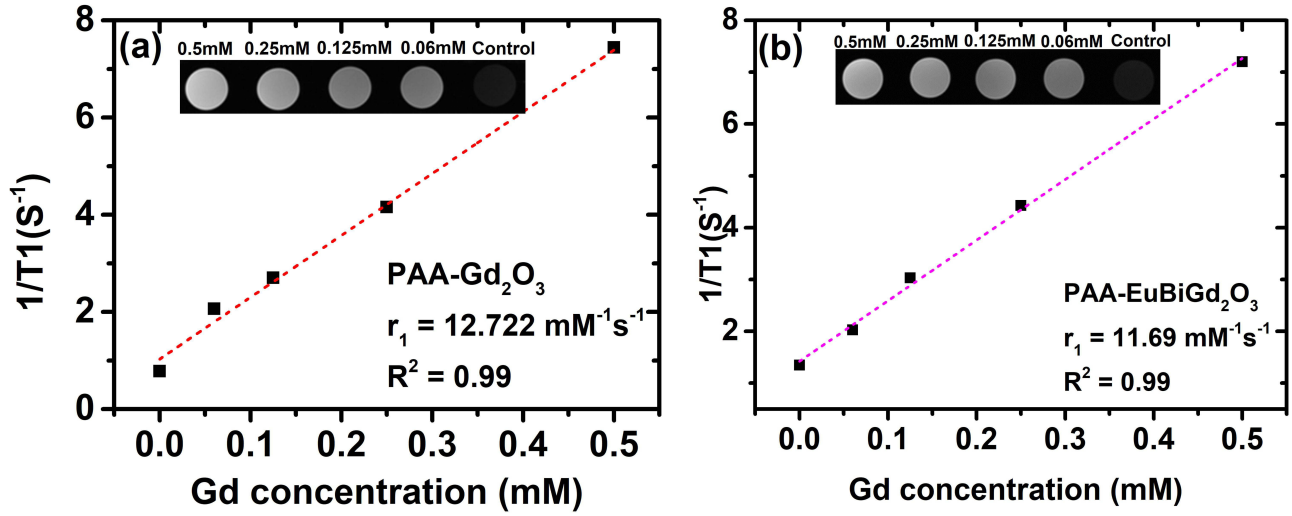

Figure 7 (**a**) Plot of inverse water-proton relaxation time (1/T1) versus Gd concentration for Gd_2O_3; and (**b**) PAA@$EuBiGd_2O_3$ concentrations in water. The slopes represent the relaxivity value r_1 ($mM^{-1}s^{-1}$).

PAA@$EuBiGd_2O_3$ are a bit lower than those of pure Gd_2O_3. This is due to replacing some Gd atoms with the Eu and Bi atoms in the nanocomposite.[99] Remarkably, the recorded r_1 values are greater than those reported for commercially available molecular Gd-chelates at 3T in water including Magnevist (3.1 L $mmol^{-1}$ s^{-1}), Gadovist (3.2 L $mmol^{-1}$ s^{-1}), Dotarem (2.8 L $mmol^{-1}$ s^{-1}), Resovist (4.6 L $mmol^{-1}$ s^{-1}), Omniscan (3.2 L $mmol^{-1}$ s^{-1}), Endorem (4.1 L $mmol^{-1}$ s^{1}) and Multihance (4.0 L $mmol^{-1}$ s^{-1}), obtained in water.[106–108] This superior relaxivity suggests that PAA@$EuBiGd_2O_3$-

https://doi.org/10.2147/IJN.S506187

NPs can achieve enhanced T1 contrast at lower doses, making them a highly promising MRI contrast agent for clinical and biomedical applications.

In vitro Cytotoxicity

The NPs were coated with biocompatible PAA to promote colloidal stability and reduce the toxicity effect of the Gd^{3+} ions, which are known to cause nephrogenic systemic fibrosis.[109,110] The biocompatibility of the PAA@EuBiGd$_2$O$_3$-NPs was investigated by measuring the cell viability of the A549 cell line using the CellTiter-Glo Luminescent Cell viability assay. The micrograph of A549 cells without the NPs treatment and after treatment with 32.5, 250, and 1000 µg/mL concentrations of PAA@EuBiGd$_2$O$_3$ NPs for 24 hrs are presented in Figure 8a–d. The cells show no significant morphological changes between the control and the NPs incubated cells for 24 hrs and 48 hrs for concentrations up to 250 µg/mL. The cell viability measured after incubation of A549 with different concentrations of the NPs in Figure 8e shows low cytotoxicity. Furthermore, the IC50 concentration of the system was determined to be 365.8 µg/mL and 337.7 µg/mL after 24 hrs and 48 hrs treatment of the cells, respectively (Figure 8f). This is higher than the IC50 of most reported gadolinium-based contrast agents.[111] These high IC50 values indicate the biocompatibility of the PAA@EuBiGd$_2$O$_3$-NPs.

The concentrations used for the MRI and fluorescence imaging are within the range of concentrations used for the cytotoxicity study. For instance, the maximum concentration used for the MRI experiment is 0.5 mM Gd, which is the same as 78.625 µg/mL (157.25 µg/mL of Gd = 1000 mM) which is lower than the IC50 value. For the fluorescence imaging, we incubated the cells with three different concentrations (125, 62.5, and 31.25 µg/mL) and found that 125 µg/mL exhibited the highest fluorescence with no observed cytotoxicity. This concentration is also lower than the IC50 value. However, for the CT imaging of the NPs inserted in the PMMA material phantom, a higher concentration of the NPs is required to obtain a visible contrast. This concentration is higher than the IC50, which may be toxic to the cells. However, in vivo toxicity animal studies need to be performed to ascertain the toxicity of the NPs.

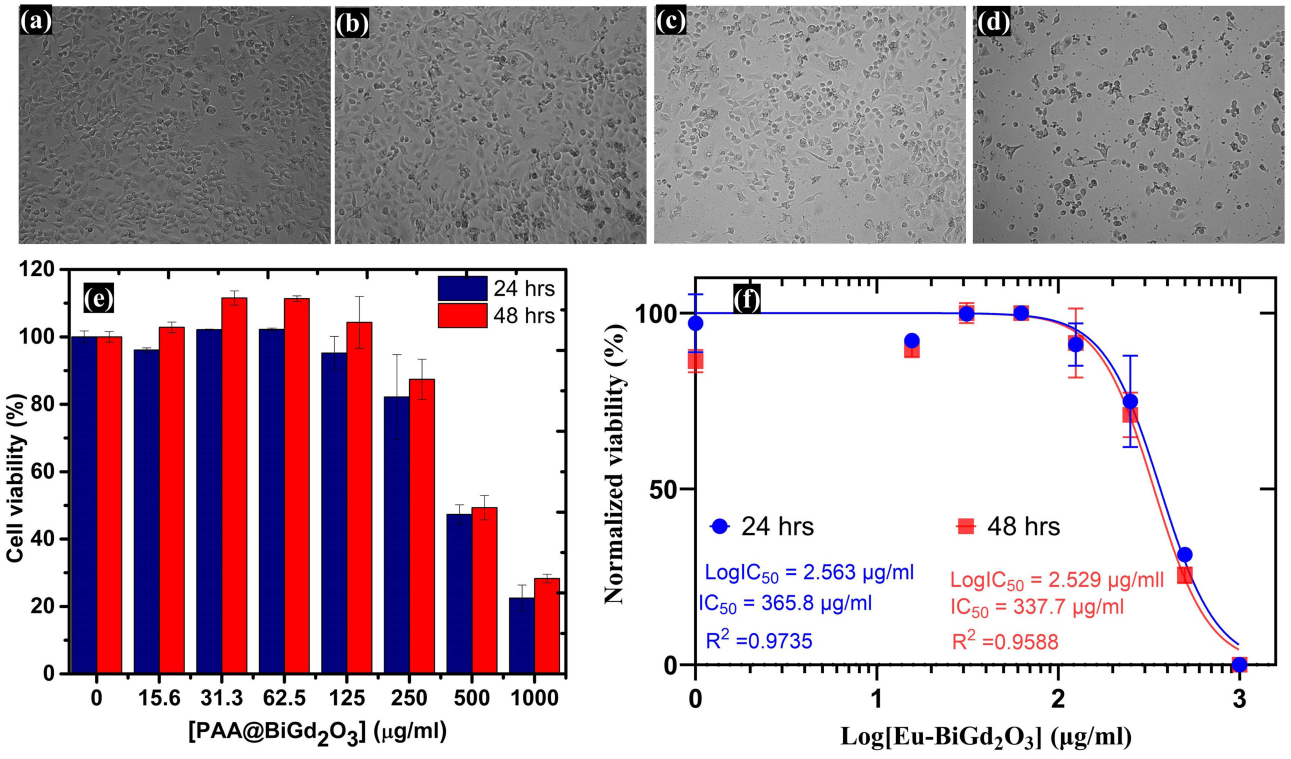

Figure 8 (**a**) A micrographs of A549 cells without NPs treatment and after treatment with PAA@EuBiGd$_2$O$_3$-NPs with concentrations of (**b**) 32.5 µg/mL, (**c**) 250 µg/mL, and (**d**) 1000 µg/mL, for 24 hrs. (**e**) CellTiter-glo based in vitro A549 cells viability studies in the presence of PAA@EuBiGd$_2$O$_3$-NPs for 24 hrs and 48 hrs. (**f**) Evaluation of IC50 after 24 hrs (365.8 µg/mL) and 48 hrs (337.8 µg/mL) treatment. The fitting correlation, R^2, values were 0.9735 and 0.9588 for 24 and 48 hrs incubation.

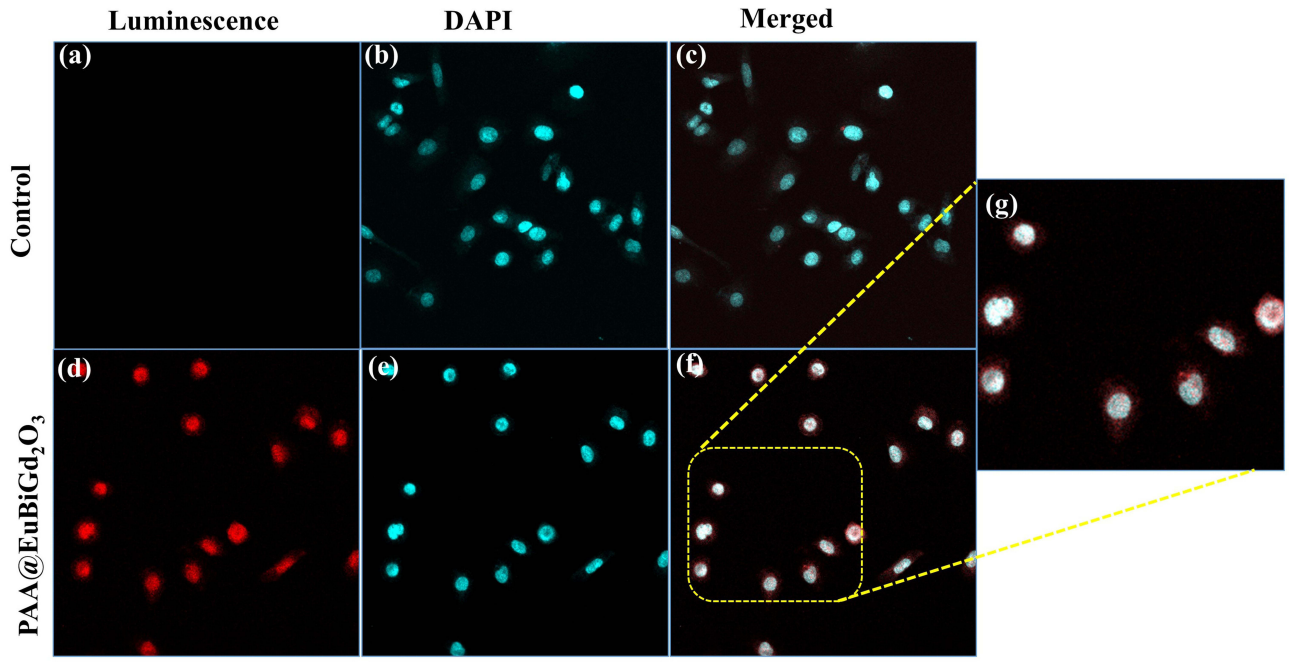

Figure 9 Confocal laser scanning microscopy images of (**a–c**) Luminescence of nanoparticles, DAPI-stained nucleus, and the merged image of untreated A549 cells. (**d–f**) Luminescence of nanoparticles, DAPI-stained nucleus, and the merged image of A549 cells treated with PAA@EuBiGd$_2$O$_3$ NPs. (**g**) Magnified view of (**f**), highlighting nanoparticle localization.

Fluorescence Imaging

The potential of the NPs as a fluorescence imaging agent was investigated using the fluorescence imaging of A549 cells. The cells were treated with PAA@EuBiGd$_2$O$_3$ NPs and imaged with confocal microscopy. Figure 9 shows the images of A549 cells obtained from the confocal microscopy. Figure 9a–c shows the luminescence of nanoparticles, DAPI-stained nuclei, and the merged image for untreated A549 cells, respectively. The untreated cells (control) show no fluorescence as expected without fluorescent dye. In contrast, Figure 9d–f presents the corresponding images for A549 cells treated with PAA@EuBiGd$_2$O$_3$ NPs, showing red fluorescence due to the presence of Eu. Interestingly, the NPs were found to be primarily localized in the cytoplasm of cells, with a small amount of the NPs attached to the nucleus (the enlarged view of the box area, Figure 9g). These observations underline the potential of PAA@EuBiGd$_2$O$_3$ NPs for use in fluorescence cell imaging.

Conclusion and Future Perspectives

A multimodal imaging agent nanostructure composite with a novel formulation PAA@EuBiGd$_2$O$_3$-NPs with an average size of 24 ± 4 nm was developed and successfully tested in an in-vitro study. Various characterization techniques confirmed the formation of PAA@EuBiGd$_2$O$_3$-NPs and their crystallinity, morphology, and optical properties. The results show high MRI contrast obtained with relaxation rates of 12.72 mM^{-1}s^{-1} and 11.77 mM^{-1}s^{-1} for Gd$_2$O$_3$ and PAA@EuBiGd$_2$O$_3$, respectively. The T1 relaxivity of PAA@EuBiGd$_2$O$_3$ is much higher than that of most commercially available MRI contrast agents such as Magnevist and Gadovist. The NPs also have high SPCCT contrast with HU versus concentration slopes of 41.5, 42.9, 59.5, and 60.8 HU mL/mg for Gd$_2$O$_3$, PAA@BiGd$_2$O$_3$, iodine, and PAA@EuBiGd$_2$O$_3$, respectively. These results prove the efficacy of the PAA@EuBiGd$_2$O$_3$ NPs as contrast agents for MRI and CT imaging. The PAA@EuBiGd$_2$O$_3$ NPs have three high-atomic number constituents of Eu, Bi, and Gd, achieving the highest slopes with significantly enhanced X-ray attenuation and image contrast. This was attributed to the synergetic effect of the composite elements and the proximity of the K-edges of Eu and Gd. In addition, the spectral CT scanner allowed us to perform material decomposition of the different NP concentrations. The toxicity study of PAA@EuBiGd$_2$O$_3$-NPs shows good biocompatibility of up to 250 µg/mL with an IC50 of 365.8 and 337.9 µg/mL for 24 and 48 hrs treatment. Furthermore, the effective delivery of the PAA@EuBiGd$_2$O$_3$-NPs

https://doi.org/10.2147/IJN.S506187

into A549 cells was verified through fluorescence microscopy imaging. The result shows that PAA@EuBiGd$_2$O$_3$-NPs have bright red fluorescence properties due to the presence of Europium in the compound. Hence, the novel biocompatible PAA@EuBiGd$_2$O$_3$-NPs have the potential for a multimodal contrast agent for cancer tissues in vivo imaging in spectral photon-counting CT and MRI and for cancer cell fluorescence imaging in vitro. Beyond cancer, the versatile imaging capabilities of PAA@EuBiGd$_2$O$_3$-NPs can be exploited for imaging other diseases, such as cardiovascular, neurological, liver, and infectious diseases, where tissue visualization is essential for diagnosis and monitoring. Future research should focus on in vivo testing of PAA@EuBiGd$_2$O$_3$-NPs to assess their clinical feasibility, image enhancement, pharmacokinetics, biodistribution, and toxicity. Integrating targeting ligands, such as folic acid and hyaluronic acid for cancer, could also improve the specificity of NPs for targeted imaging, enhancing their applicability in various medical applications.

Acknowledgments

The authors would like to acknowledge the support of the Department of Physics, Chemistry, and the Advanced Materials Chemistry Centre (AMCC) at Khalifa University. This project was funded by the Khalifa University of Science and Technology, Abu Dhabi, UAE, under grant number 8474000366 (000160 - Khalifa University - FSU). We also acknowledge the financial support from Al Jalila Foundation (No. AJF2023-175) and SANDOOQ AL WATAN (SWARD) grant under PRJ-SWARD-691. The MRI studies were conducted at the Brain Imaging Core Technology Platforms lab at New York University Abu Dhabi.

Disclosure

The authors report no conflicts of interest in this work.

References

1. Siegel RL, Miller KD, Jemal A. Cancer statistics, 2020. *CA Cancer J Clin*. 2020;70(7):1.
2. Siegel RL, Giaquinto AN, Jemal A. Cancer statistics, 2024. *CA Cancer J Clin*. 2024;12:1.
3. Han X, Xu K, Taratula O, Farsad K. Applications of nanoparticles in biomedical imaging. *Nanoscale*. 2019;11:799. doi:10.1039/C8NR07769J
4. Hussain S, Mubeen I, Ullah N, et al. Modern diagnostic imaging technique applications and risk factors in the medical field: a review. *BioMed Res Int*. 2022;2022:5164970. doi:10.1155/2022/5164970
5. Si-Mohamed S, Bar-Ness D, Sigovan M, et al. Multicolour imaging with spectral photon-counting CT: a phantom study. *Eur Radiol Exp*. 2018;2(34). doi:10.1186/s41747-018-0063-4
6. Wu M, Xue Y, Li N, et al. Tumor-microenvironment-induced degradation of ultrathin gadolinium oxide nanoscrolls for magnetic-resonance-imaging-monitored, activatable cancer chemotherapy. *Angew Chem Int Ed Engl*. 2019;58:6880. doi:10.1002/anie.201812972
7. Cheng C-A, Chen W, Zhang L, Wu HH, Zink JI. A responsive mesoporous silica nanoparticle platform for magnetic resonance imaging-guided high-intensity focused ultrasound-stimulated cargo delivery with controllable location, time, and dose. *J Am Chem Soc*. 2019;141:17670. doi:10.1021/jacs.9b07591
8. Liu N, Marin R, Mazouzi Y, Cron GO, Shuhendler A, Hemmer E. Cubic versus hexagonal – effect of host crystallinity on the T1 shortening behaviour of NaGdF4 nanoparticles. *Nanoscale*. 2019;11:6794. doi:10.1039/C9NR00241C
9. Yang J, Zhao Q, Zang Z, et al. A dual-mode T1 MRI/CT contrast agent of Gd2O3/Au@MSNs for tumor imaging with high performance. *Materialia*. 2022;24:101494.
10. Glunde K, Artemov D, Penet M-F, Jacobs MA, Bhujwalla ZM. Magnetic resonance spectroscopy in metabolic and molecular imaging and diagnosis of cancer. *Chem Rev*. 2010;110:3043. doi:10.1021/cr9004007
11. Xia H-X, Yang X-Q, Song J-T, et al. Folic acid-conjugated silica-coated gold nanorods and quantum dots for dual-modality CT and fluorescence imaging and photothermal therapy. *J Mater Chem B*. 2014;2:1945. doi:10.1039/c3tb21591a
12. Lee D-E, Koo H, Sun I-C, Ryu JH, Kim K, Kwon IC. Multifunctional nanoparticles for multimodal imaging and theragnosis. *Chem Soc Rev*. 2012;41:2656. doi:10.1039/c2cs15261d
13. Pysz MA, Gambhir SS, Willmann JK. Molecular imaging: current status and emerging strategies. *Clin Radiol*. 2010;65:500. doi:10.1016/j.crad.2010.03.011
14. Wang G, Gao W, Zhang X, Mei X. Au nanocage functionalized with ultra-small Fe3O4 nanoparticles for targeting T1-T2 dual MRI and CT imaging of tumor. *Sci Rep*. 2016;6(1):28258.
15. Zhang Y, Jeon M, Rich LJ, et al. Non-invasive multimodal functional imaging of the intestine with frozen micellar naphthalocyanines. *Nat Nanotechnol*. 2014;9:631. doi:10.1038/nnano.2014.130
16. Kim T, Hyeon T. Applications of inorganic nanoparticles as therapeutic agents. *Nanotechnology*. 2013;25:12001. doi:10.1088/0957-4484/25/1/012001
17. McNamara K, Tofail SAM. Nanoparticles in Biomedical Applications. *Adv Phys X*. 2017;2:54.
18. Ramos AP, Cruz MAE, Tovani CB, Ciancaglini P. Biomedical applications of nanotechnology. *Biophys Rev*. 2017;9:79. doi:10.1007/s12551-016-0246-2
19. Zhou Z, Zhang S, Xue N. Research progress of cancer cell membrane coated nanoparticles for the diagnosis and therapy of breast cancer. *Front Oncol*. 2023;13. doi:10.3389/fonc.2023.1270407

20. Rajana N, Mounika A, Chary PS, et al. Multifunctional hybrid nanoparticles in diagnosis and therapy of breast cancer. *J Control Release*. 2022;352:1024. doi:10.1016/j.jconrel.2022.11.009
21. Hegde M, Naliyadhara N, Unnikrishnan J, et al. Nanoparticles in the diagnosis and treatment of cancer metastases: current and future perspectives. *Cancer Lett*. 2023;556:216066.
22. Fernandes DA. Review on metal-based theranostic nanoparticles for cancer therapy and imaging. *Technol Cancer Res Treat*. 2023;22:15330338231191493.
23. Sun L, Liu H, Ye Y, et al. Smart Nanoparticles for Cancer Therapy. *Signal Transduct Target Ther*. 2023;8:418. doi:10.1038/s41392-023-01642-x
24. Fernandes DA. Theranostic polymeric nanoparticles for cancer. *BioNanoScience*. 2023;13(4):1609–1644.
25. Boros E, Packard AB. Radioactive transition metals for imaging and therapy. *Chem Rev*. 2019;119:870. doi:10.1021/acs.chemrev.8b00281
26. Gupta A, Caravan P, Price WS, Platas-Iglesias C, Gale EM. Applications for Transition-Metal Chemistry in Contrast-Enhanced Magnetic Resonance Imaging. *Inorg Chem*. 2020;59:6648. doi:10.1021/acs.inorgchem.0c00510
27. Peng Q, Qian Z, Gao H, Zhang K. Recent advances in transition-metal based nanomaterials for noninvasive oncology thermal ablation and imaging diagnosis. *Front Chem*. 2022;10(1). doi:10.3389/fchem.2022.899321
28. Rahmani AA, Jia Q, Bahti HH, Fauzia RP, Wyantuti S. Recent advances in lanthanide-based nanoparticle contrast agents for magnetic resonance imaging: synthesis, characterization, and applications. *OpenNano*. 2025;21:100226.
29. Bottrill M, Kwok L, Long NJ. Lanthanides in magnetic resonance imaging. *Chem Soc Rev*. 2006;35:557. doi:10.1039/b516376p
30. Laurent S, Vander Elst L, Muller RN. Lanthanide complexes for magnetic resonance and optical molecular imaging. *Q J Nucl Med Mol Imaging*. 2009;53:586.
31. Debroye E, Parac-Vogt TN. Towards polymetallic lanthanide complexes as dual contrast agents for magnetic resonance and optical imaging. *Chem Soc Rev*. 2014;43:8178. doi:10.1039/C4CS00201F
32. Dunning CAS, O'Connell J, Robinson SM, et al. Photon-counting computed tomography of lanthanide contrast agents with a high-flux 330-Mm-pitch cadmium zinc telluride detector in a table-top system. *J Med Imaging*. 2020;7:33502.
33. Park JY, Chang Y, Lee GH. Multi-modal imaging and cancer therapy using lanthanide oxide nanoparticles: current status and perspectives. *Curr Med Chem*. 2015;22:569. doi:10.2174/0929867322666141128162843
34. Fernandes DA. Review on iron nanoparticles for cancer theranostics: synthesis, modification, characterization and applications. *J Nanopart Res*. 2023;25(8):170.
35. Sanchez LM, Martin DA, Alvarez VA, Gonzalez JS. Polyacrylic acid-coated iron oxide magnetic nanoparticles: the polymer molecular weight influence. *Colloids Surf A*. 2018;543:28.
36. Arkaban H, Khajeh Ebrahimi A, Yarahmadi A, Zarrintaj P, Barani M. Development of a multifunctional system based on CoFe(2)O(4) @polyacrylic acid NPs conjugated to folic acid and loaded with doxorubicin for cancer theranostics. *Nanotechnology*. 2021;32.
37. Arkaban H, Barani M, Akbarizadeh MR, et al. Polyacrylic acid nanoplatforms: antimicrobial, tissue engineering, and cancer theranostic applications. *Polymers*. 2022;14.
38. Adelnia H, Blakey I, Little PJ, Ta HT. Hydrogels based on Poly(Aspartic Acid): synthesis and applications. *Front Chem*. 2019;7(1).
39. Marasini S, Yue H, Ghazanfari A, et al. Polyaspartic acid-coated paramagnetic gadolinium oxide nanoparticles as a dual-modal T1 and T2 magnetic resonance imaging contrast agent. *Appl Sci*. 2021;11:8222.
40. Vega-Chacón J, Arbeláez MIA, Jorge JH, Marques RFC, Jafelicci MJ. PHResponsive Poly(Aspartic Acid) hydrogel-coated magnetite nanoparticles for biomedical applications. *Mater Sci Eng C Mater Biol Appl*. 2017;77:366. doi:10.1016/j.msec.2017.03.244
41. Vega-Chacón J, Arbeláez MIA, Jorge JH, Marques RFC, Jafelicci M. PHResponsive Poly(Aspartic Acid) hydrogel-coated magnetite nanoparticles for biomedical applications. *Mater Sci Eng C*. 2017;77:366.
42. Liu Q, Liu L, Mo C, et al. Polyethylene glycol-coated ultrasmall superparamagnetic iron oxide nanoparticles coupled sialyl Lewis X nanotheranostic platform for nasopharyngeal carcinoma imaging and photothermal therapy. *J Nanobiotechnology*. 2021;19:171. doi:10.1186/s12951-021-00918-0
43. Dougherty A, Nasution ELY, Iskandar F, Dougherty G. Facile solvothermal synthesis and functionalization of polyethylene glycol-coated paramagnetic Gd2(CO3)3 particles and corresponding Gd2O3 nanoparticles for use as MRI contrast agents. *J Sci Adv Mater Devices*. 2019;4:72.
44. Fortin MA, Petoral RM, Söoderlind F, et al. Polyethylene glycol-covered ultra-small Gd2O3 nanoparticles for positive contrast at 1.5 T magnetic resonance clinical scanning. *Nanotechnology*. 2007;18:395501. doi:10.1088/0957-4484/18/39/395501
45. Liu H, Zhang M, Meng F, Su C, Li J. Polysaccharide-based gold nanomaterials: synthesis mechanism, polysaccharide structure-effect, and anticancer activity. *Carbohydr Polym*. 2023;321:121284. doi:10.1016/j.carbpol.2023.121284
46. Uthaman S, Lee SJ, Cherukula K, Cho C-S, Park I-K. Polysaccharide-coated magnetic nanoparticles for imaging and gene therapy. *BioMed Res Int*. 2015;2015:959175. doi:10.1155/2015/959175
47. Tokumitsu H, Ichikawa H, Fukumori Y. Chitosan-gadopentetic acid complex nanoparticles for gadolinium neutron-capture therapy of cancer: preparation by novel emulsion-droplet coalescence technique and characterization. *Pharma Res*. 1999;16:1830. doi:10.1023/A:1018995124527
48. Cheng -J-J, Zhu J, Liu X-S, et al. Gadolinium-chitosan nanoparticles as a novel contrast agent for potential use in clinical bowel-targeted MRI: a feasibility study in healthy rats. *Acta Radiol*. 2012;53:900. doi:10.1258/ar.2012.110017
49. Alkilany AM, Rachid O, Alkawareek MY, Billa N, Daou A, Murphy CJ. PLGAGold nanocomposite: preparation and biomedical applications. *Pharmaceutics*. 2022;14:660. doi:10.3390/pharmaceutics14030660
50. Kumar A, Kumar A. Chapter 7 - Poly(Lactic Acid) and Poly(Lactic-Co-Glycolic) acid nanoparticles: versatility in biomedical applications. In: Grumezescu V, Grumezescu AM, editors. *Materials for Biomedical Engineering*. Elsevier; 2019:199–216.
51. Xu J, Wan K, Wang H, et al. Polyethylenimine–Poly(Lactic-Co-Glycolic Acid)2 nanoparticles show an innate targeting ability to the submandibular salivary gland via the muscarinic 3 receptor. *ACS Cent Sci*. 2021;7:1938. doi:10.1021/acscentsci.1c01083
52. Swy ER, Schwartz-Duval AS, Shuboni DD, et al. Dual-modality, fluorescent, PLGA encapsulated bismuth nanoparticles for molecular and cellular fluorescence imaging and computed tomography. *Nanoscale*. 2014;6:13104. doi:10.1039/C4NR01405G
53. Kumar Y, Sinha ASK, Nigam KDP, Dwivedi D, Sangwai JS. Functionalized nanoparticles: tailoring properties through surface energetics and coordination chemistry for advanced biomedical applications. *Nanoscale*. 2023;15:6075. doi:10.1039/d2nr07163k

54. Gao Y, Wang K, Zhang J, Duan X, Sun Q, Men K. Multifunctional Nanoparticle for Cancer Therapy. *MedComm*. 2023;4:e187. doi:10.1002/mco2.187
55. Das MK, Pathak YV. Nano medicine and nano safety. 2020.
56. Si-Mohamed S, Cormode DP, Bar-Ness D, et al. Evaluation of spectral photon counting computed tomography KEdge imaging for determination of gold nanoparticle biodistribution in vivo. *Nanoscale*. 2017;9:18246. doi:10.1039/C7NR01153A
57. Pan D, Schirra CO, Senpan A, et al. An early investigation of ytterbium nanocolloids for selective and quantitative "Multicolor" spectral CT imaging. *ACS Nano*. 2012;6:3364. doi:10.1021/nn300392x
58. Schirra CO, Brendel B, Anastasio MA, Roessl E. Spectral CT: a technology primer for contrast agent development. *Contrast Media Mol Imaging*. 2014;9:62.
59. Fu JJ, Guo -J-J, Qin A-P, et al. Bismuth chelate as a contrast agent for X-ray computed tomography. *J Nanobiotechnology*. 2020;18(1). doi:10.1186/s12951-020-00669-4
60. Charczuk N, Targońska S, Zákutná D, Watras A, Patej A, Wiglusz RJ. Europium(III) and Gadolinium(III) Co-Doped nanohydroxyapatite with enhanced photoluminescence as potential multimodal bioimaging agent. *Ceram Int*. 2024;50:14601. doi:10.1016/j.ceramint.2024.01.372
61. Pinho SLC, Sereno J, Abrunhosa AJ, et al. Gd- and Eu-loaded iron Oxide@Silica core–shell nanocomposites as trimodal contrast agents for magnetic resonance imaging and optical imaging. *Inorg Chem*. 2019;58:16618. doi:10.1021/acs.inorgchem.9b02655
62. Zhu G, Chen L, Zeng F, et al. GdVO4:Eu3+,Bi3+ nanoparticles as a contrast agent for MRI and luminescence bioimaging. *ACS Omega*. 2019;4:15806. doi:10.1021/acsomega.9b00444
63. Wang GD, Chen H, Tang W, Lee D, Xie J. Gd and Eu Co-doped nanoscale metal– organic framework as a T1–T2 dual-modal contrast agent for magnetic resonance imaging. *Tomography*. 2016;2:179. doi:10.18383/j.tom.2016.00226
64. Atabaev TS, Lee JH, Shin YC, et al. Eu, Gd-Codoped yttria nanoprobes for optical and T1-weighted magnetic resonance imaging. *Nanomaterials*. 2017;7:35. doi:10.3390/nano7020035
65. Deng H, Chen F, Yang C, Chen M, Li L, Chen D. Effect of Eu doping concentration on fluorescence and magnetic resonance imaging properties of Gd2O3:Eu3+ nanoparticles used as dual-modal contrast agent. *Nanotechnology*. 2018;29:415601. doi:10.1088/1361-6528/aad347
66. Perdigon-Lagunes P, Estevez O, Zorrilla Cangas C, Herrera-Becerra R. Gd - Gd2O3 multimodal nanoparticles as labeling agents. *MRS Adv*. 2018;3:761.
67. Yang C-T, Hattiholi A, Selvan ST, et al. Gadolinium-based bimodal probes to enhance T1-weighted magnetic resonance/optical imaging. *Acta Biomater*. 2020;110:15. doi:10.1016/j.actbio.2020.03.047
68. Wang X, Chan HN, Desbois N, et al. Multimodal theranostic cyanine-conjugated Gadolinium(III) complex for in vivo imaging of amyloid-β in an Alzheimer's disease mouse model. *ACS Appl Mater Interfaces*. 2021;13:18525.
69. Song B, Li M, Ren J, et al. A multifunctional nanoprobe based on Europium(Iii) complex–Fe3O4 nanoparticles for bimodal time-gated luminescence/magnetic resonance imaging of cancer cells in vitro and in vivo. *New J Chem*. 2022;46:9658.
70. Fang F, Zhao D, Zhang Y, Li M, Ye J, Zhang J. Europium-doped nanoparticles for cellular luminescence lifetime imaging via multiple manipulations of aggregation state. *ACS Appl Bio Mater*. 2020;3:5103. doi:10.1021/acsabm.0c00580
71. Ge J, Li C, Wang N, et al. Effects of PEG chain length on relaxometric properties of iron oxide nanoparticles-based MRI contrast agent. *Nanomaterials*. 2022;12:2673. doi:10.3390/nano12152673
72. Cruje C, Dunmore-Buyze PJ, Grolman E, Holdsworth DW, Gillies ER, Drangova M. PEG-modified gadolinium nanoparticles as contrast agents for in vivo MicroCT. *Sci Rep*. 2021;11(1).
73. Alzoubi FY, Abu Noqta O, Al Zoubi T, et al. A novel one-pot synthesis of PVP-coated iron oxide nanoparticles as biocompatible contrast agents for enhanced T2-weighted MRI. *J Compos Sci*. 2023;7.
74. Fang J, Chandrasekharan P, Liu X-L, et al. Manipulating the surface coating of ultra-small Gd2O3 nanoparticles for improved T1Weighted MR imaging. *Biomaterials*. 2014;35(5):1636–1642. doi:10.1016/j.biomaterials.2013.11.032
75. Miao X, Ho SL, Tegafaw T, et al. Stable and non-toxic ultrasmall gadolinium oxide nanoparticle colloids (Coating Material = Polyacrylic Acid) as high-performance: t 1 magnetic resonance imaging contrast agents. *RSC Adv*. 2018;8:3189. doi:10.1039/C7RA11830A
76. Ho SL, Cha H, Oh IT, et al. Magnetic resonance imaging, gadolinium neutron capture therapy, and tumor cell detection using ultrasmall Gd2O3 nanoparticles coated with polyacrylic acid-rhodamine B as a multifunctional tumor theragnostic agent. *RSC Adv*. 2018;8:12653. doi:10.1039/c8ra00553b
77. Yim ES, Zhao B, Myung D, et al. Biocompatibility of Poly(Ethylene Glycol)/Poly(Acrylic Acid) interpenetrating polymer network hydrogel particles in RAW 264.7 macrophage and MG-63 osteoblast cell lines. *J Biomed Mater Res Part A*. 2009;91A:894.
78. Aamir R, Chernoglazov A, Bateman CJ, et al. Mars spectral molecular imaging of lamb tissue: data collection and image analysis. *J Instrum*. 2014;9.
79. Ballabriga R, Alozy J, Blaj G, et al. The Medipix3RX: a high resolution, zero dead-time pixel detector readout chip allowing spectroscopic imaging. *J Instrum*. 2013;8:C02016.
80. Tang ND, de Ruiter N, Mohr JL, Butler APH, Butler PH, Aamir R. Using algebraic reconstruction in computed tomography. In: *Proceedings of the 27th Conference on Image and Vision Computing New Zealand*. New York, NY, USA: Association for Computing Machinery; 2012:216–221.
81. Baer K, Kieser S, Schon B, et al. Spectral CT imaging of human osteoarthritic cartilage via quantitative assessment of glycosaminoglycan content using multiple contrast agents. *APL Bioeng*. 2021;5:26101. doi:10.1063/5.0035312
82. Moghiseh M, Lowe C, Lewis JG, et al. Spectral photon-counting molecular imaging for quantification of monoclonal antibody-conjugated gold nanoparticles targeted to lymphoma and breast cancer: an in vitro study. *Contrast Media Mol Imaging*. 2018;2018.
83. Marfo E, Anderson NG, Butler AP, et al. Assessment of material identification errors, image quality, and radiation doses using small animal spectral photon-counting CT. *IEEE Trans Radiat Plasma Med Sci*. 2021;5:578.
84. Kong W, Yue Q, Li Q, Gao B. Adsorption of Cd 2+ on GO/PAA hydrogel and preliminary recycle to GO/PAA-CdS as efficient photocatalyst. *Sci Total Environ*. 2019;668:1165. doi:10.1016/j.scitotenv.2019.03.095
85. Ismail O, Beyribey B, Turhan K. Removal of water in liquid fuel with a super absorbent copolymer. *Energy Sources Part A*. 2011;33:1669. doi:10.1080/15567030903436855

86. Ho SL, Choi G, Yue H, et al. In vivo neutron capture therapy of cancer using ultrasmall gadolinium oxide nanoparticles with cancer-targeting ability. *RSC Adv*. 2019;10:865. doi:10.1039/C9RA08961F
87. Ho SL, Choi G, Yue H, et al. In vivo neutron capture therapy of cancer using ultrasmall gadolinium oxide nanoparticles with cancer-targeting ability. *RSC Adv*. 2020;10:865.
88. Mendive CB, Bredow T, Blesa MA, Bahnemann DW. ATR-FTIR measurements and quantum chemical calculations concerning the adsorption and photoreaction of oxalic acid on TiO2. *Phys Chem Chem Phys*. 2006;8:3232. doi:10.1039/b518007b
89. Duckworth OW, Martin ST. Surface complexation and dissolution of hematite by C1-C6 dicarboxylic acids at PH = 5.0. *Geochim Cosmochim Acta*. 2001;65:4289.
90. Hug SJ, Bahnemann D. Infrared spectra of oxalate, malonate and succinate adsorbed on the aqueous surface of rutile, anatase and lepidocrocite measured with in situ ATR-FTIR. *J Electron Spectros Relat Phenomena*. 2006;150:208.
91. Wiśniewska M, Terpiłowski K, Chibowski S, Urban T, Zarko VI, Gun'ko VM. Effect of Polyacrylic Acid (PAA) adsorption on stability of mixed alumina-silica oxide suspension. *Powder Technol*. 2013;233:190.
92. Souza TGF, Ciminelli VST, Mohallem NDS. A comparison of TEM and DLS methods to characterize size distribution of ceramic nanoparticles. *J Phys Conf Ser*. 2016;733:012039. doi:10.1088/1742-6596/733/1/012039
93. Wu C, Cai R, Zhao T, et al. Hyaluronic acid-functionalized gadolinium oxide nanoparticles for magnetic resonance imaging-guided radiotherapy of tumors. *Nanoscale Res Lett*. 2020;15. doi:10.1186/s11671-020-03318-9
94. Zhang N, Chen D, Niu F, Wang S, Qin L, Huang Y. Enhanced visible light photocatalytic activity of Gd-Doped BiFeO3 nanoparticles and mechanism insight. *Sci Rep*. 2016;6(1).
95. Kumar S, Prakash R, Singh V. Synthesis, characterization, and applications of europium oxide: a review. *Rev Adv Sci Eng*. 2016;4:247.
96. Kumar S, Prakash R, Choudhary RJ, Phase DM. Structural, XPS and magnetic studies of pulsed laser deposited Fe doped Eu2O3 thin film. *Mater Res Bull*. 2015;70:392.
97. Zeng C-H, Zheng K, Lou K-L, et al. Synthesis of porous europium oxide particles for photoelectrochemical water splitting. *Electrochim Acta*. 2015;165:396.
98. Ullah N, Imran M, Liang K, et al. Highly dispersed ultra-small Pd nanoparticles on gadolinium hydroxide nanorods for efficient hydrogenation reactions. *Nanoscale*. 2017;9:13800. doi:10.1039/c7nr05096h
99. Maalej NM, Qurashi A, Assadi AA, et al. Synthesis of Gd2O3:Eu nanoplatelets for MRI and fluorescence imaging. *Nanoscale Res Lett*. 2015;10. doi:10.1186/s11671-015-0905-4
100. Verma T, Agrawal S. Photoluminescent and thermoluminescent studies of Dy3+ and Eu3+ doped Y2O3 phosphors. *J Fluoresc*. 2018;28:453. doi:10.1007/s10895-018-2208-5
101. De almeida R, da Silva DM, Kassab LRP, de Araújo CB. Eu3+ luminescence in tellurite glasses with gold nanostructures. *Opt Commun*. 2008;281:108.
102. Ruvalcaba-Cornejo C, Lozada-Morales R, Zayas ME, Rincón JM, Marquez H, Flores ADL. Effect of the 3+ addition on photoluminescence and microstructure of —2 glasses. *J Am Ceram Soc*. 2013;96:3084.
103. Dehelean A, Rada S, Popa A, Suciu RC, Culea E. Raman, photoluminescence and EPR spectroscopic characterization of Europium(III) oxide–lead dioxide–tellurite glassy network. *J Lumin*. 2016;177:65.
104. Moghiseh M, Searle E, Dixit D, et al. Spectral photon-counting CT imaging of gold nanoparticle labelled monocytes for detection of atherosclerosis: a preclinical study. *Diagnostics*. 2023;13:499. doi:10.3390/diagnostics13030499
105. Ibrahim YO, Maalej N, Masood Pirzada B, et al. Gold nanoparticles spectral CT imaging and limit of detectability in a new materials contrast-detail phantom. *Phys Medica*. 2024;120:103326. doi:10.1016/j.ejmp.2024.103326
106. Wahsner J, Gale EM, Rodríguez-Rodríguez A, Caravan P. Chemistry of MRI contrast agents: current challenges and new frontiers. *Chem Rev*. 2019;119:957. doi:10.1021/acs.chemrev.8b00363
107. Caravan P, Ellison JJ, McMurry TJ, Lauffer RB. Gadolinium(III) Chelates as MRI contrast agents: structure, dynamics, and applications. *Chem Rev*. 1999;99:2293. doi:10.1021/cr980440x
108. Rohrer M, Bauer H, Mintorovitch J, Requardt M, Weinmann HJ. Comparison of magnetic properties of MRI contrast media solutions at different magnetic field strengths. *Invest Radiol*. 2005;40:715. doi:10.1097/01.rli.0000184756.66360.d3
109. Ramalho J, Ramalho M, Jay M, Burke LM, Semelka RC. Gadolinium toxicity and treatment. *Magn Reson Imaging*. 2016;34:1394. doi:10.1016/j.mri.2016.09.005
110. Thomsen HS. *Nephrogenic Systemic Fibrosis: A Serious Late Adverse Reaction to Gadodiamide*. European Radiology; 2006.
111. Aouidat F, Boumati S, Khan M, Tielens F, Doan B-T, Spadavecchia J. Design and synthesis of gold-gadolinium-core-shell nanoparticles as contrast agent: a smart way to future nanomaterials for nanomedicine applications. *Int J Nanomed*. 2019;14:9309. doi:10.2147/IJN.S224805